INTERNATIONAL JOURNAL FOR NUMERICAL METHODS IN FLUIDS
Int. J. Numer. Meth. Fluids 2003; **41**:765–788 (DOI: 10.1002/fld.470)

Numerical simulation of thermo-solutal-capillary migration of a dissolving drop in a cavity

Edmondo Bassano*,†

MARS Center, Via E. Gianturco 31, I-80146 Napoli, Italy

SUMMARY

In the present paper the thermo-solutal-capillary migration of a dissolving liquid drop, composed by a binary mixture having a miscibility gap, injected in a closed cavity with differentially heated end walls, is studied. The main goal of the analysis is to clarify if and how the drop migration is affected by the dissolution process. The numerical code is based on a finite volume formulation. A level-set technique is used for describing the dynamics of the interface separating the different phases. A thermodynamic constraint fixes the concentration jump between the interface sides. This jump, together with that of the concentration normal derivatives, in turn defines the entity of the dissolution cross-flow through the interface and the interface velocity relative to the fluid. Since the jump singularity of normal derivatives cannot be easily mollified, while retaining the necessary accuracy, a scheme for the species equation is elaborated that allows sharp jumps and has subcell resolution. Steady migration speeds are determined after the start-up phase for different radii and temperature differences. The results will be used for the preparation of a sounding rocket space experiment. Copyright © 2003 John Wiley & Sons, Ltd.

KEY WORDS: level set; drop migration; miscibility gap; thermo-solutal capillary convection; cavity

1. INTRODUCTION

Processes based on phase changes are of primary interest in physics and engineering. This explains the interest of the scientific community on miscibility gap [1, 2] as well as closely related phenomena. A search on the IDEA database (http://mgravity.itsc.uah.edu/ideasearch.html) using the 'miscibility gap' keyword returned over 70 items of experiments flown in microgravity conditions. The experiments covered more than two decades and flew on almost every kind of microgravity platform. A miscibility gap in the liquid phase is found in many different systems: metal alloys, binary mixtures of organic liquids, sulphides and silicates systems, glasses and liquid crystals and many of industrial applications and processes are based on miscibility gap and related phenomena, an account can be found in Bassano (MARS internal report 'Welcome/FR-001', 2000). The dissolution due to a miscibility gap and its influence

* Correspondence to: E. Bassano, MARS Center, Via E. Gianturco 31, I-80146 Napoli, Italy.
† E-mail: bassano@marscenter.it

Received March 2002
Revised 1 November 2002

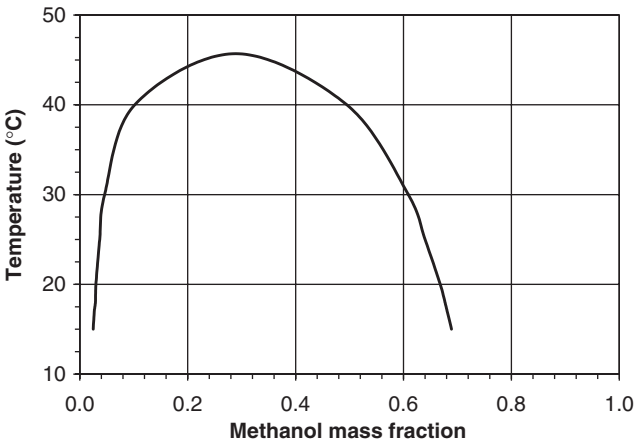

Figure 1. Cyclohexane–methanol phase diagram.

on capillary migration of drops can be profitably studied in microgravity, being strongly affected, on Earth, by buoyancy due to both different densities of the mixture components and Boussinesq effects.

The system under study is composed by two liquid binary mixtures of the same components having a miscibility gap, i.e. coexisting in a given range of temperature in two different phases at different concentrations. A drop of a pure component is injected in a matrix of the other component, that fills a closed rectangular cavity and has a linearly stratified temperature. The upper and lower walls are held at constant different temperatures. The system is supposed to be in absence of gravity, therefore only interfacial tension gradient effects occur. The drop migrates towards the hot upper wall because of the solutal and thermal Marangoni effect and dissolves because the system is in a region of the phase diagram where it separates continuously into two phases, according to the equilibrium curve.

The couple of liquids exhibiting a first order phase transition used for the simulations is cyclohexane (C_6H_{12})–methanol (CH_3OH). This couple has been selected because: (i) the components have nearly the same density; (ii) are transparent, allowing either the direct visualization of the drop migration either the use of optical diagnostics devices; (iii) their mixture has a critical temperature of 45.7°C, slightly larger than the ambient one. Theoretical models for calculating the equilibrium curve are available and are particularly helpful for ideal solutions, but differences in atomic radius and in bonding are responsible for eventually large discrepancies between real and ideal behaviour [1], thus the cyclohexane–methanol equilibrium phase diagram, shown in Figure 1, is given by points. It is supposed that equilibrium always occurs at the binodal line.

Some of the restrictive hypotheses largely adopted in the classical theoretical and numerical literature on thermo-capillary migration of bubbles and drops [3–8] are removed in the present paper. The flow develops in a cavity and not in an unbounded medium so that the boundary conditions for the external phase are correctly imposed. This circumstance avoids the problem of relating experimental results to simulations with suitably adapted boundary conditions, reproduces the exact flow topology in which the particles paths do not come from and go to infinity and are instead folded over the immersed phase, and allows one to evaluate wall

effects (drop diameter of the same order of the smaller cavity characteristic length, drop near the wall). The simulation is unsteady and models the start-up phase of the drop that can change its shape freely and is not constrained to remain spherical during the migration. The interface is crossed by mass. The scheme for the specie equation allows one to treat finite jumps and the average based flux reconstruction on variable length stencils is not constrained to be first order accurate in cells where a jump occurs.

In recent years several different methods for solving multiphase flows were elaborated, among them we recall marker and cells [9], volume of fluid [10], front tracking [11], boundary integral [12]. An account of the more extensively used numerical methods, issues and problems related to free surface and two-phase flows can be found in Reference [13]. Nevertheless the severe limitations of all these methods did not match all the constraints of the present problem.

A first milestone work, on which several numerical approaches would successively rely, was the work of Brackbill *et al.* [14]. Here the authors introduced a formulation of multiphase flows equations in terms of a unique system of motion equations holding in the whole domain, expressed the interface normal momentum boundary condition in the case of constant surface tension as a momentum production term, and finally used a color function to identify different phases.

Their work and the projection method of Chorin [15] and Temam [16], subsequently inspired Bell and Marcus [17], in formulating the Hodge-like projection for variable density incompressible multiphase flows. Later on several authors upgraded these formulations in terms of accuracy. Extension to non-constant surface tension was made by Haj-Hariri *et al.* [8].

In their landmark paper Osher and Sethian [18] introduced the level set method for modelling fronts, that, treating implicitly the moving boundary, allowed front topological changes without elaborated machinery or failure of many other front dynamics description methods. From that moment, level set methods have been applied in all fields. The first application to multiphase flow is of Sussman *et al.* [19]. Phase changes of pure substances were taken into account by Beux *et al.* [20] and, in the context and front tracking methods, by Tryggvason *et al.* [21], Brackbill *et al.* [22] and Esmaeeli *et al.* [23]. The same authors [24, 25] studied also multiphase flow of mixtures.

In the present paper the drop interface evolution is modelled by the level set technique, in which the interface is represented by the embedding of the zero level set of a scalar function defined within the whole computational domain. The present simulations are part of the preparation of an experiment on the thermo-solutal-capillary migration of a dissolving drop, which will be flown onboard sounding rocket MAXUS 5 in spring 2003 [26].

2. THE LEVEL SET METHOD

The level set method for advancing fronts was proposed by Osher and Sethian [18]. The front, in our case the interface $\gamma(t)$, is represented at each instant of time t by the zero level set of a smooth scalar function ϕ. Let $x(t)$ be a representation of $\gamma(t)$ and $V_i(t) = \dot{x}(t)$. The evolution equation for ϕ is described by the scalar equation of Hamilton–Jacoby type

$$\phi_t + V_i \cdot \nabla\phi = \phi_t + V_{\text{in}}|\nabla\phi| = 0 \tag{1}$$

for this equation states that, if at the initial time ϕ is constant along the curve γ moving in normal direction with speed $V_{\text{in}} = n \cdot V_i$, it will be constant there also at later times. In the

second equality above the unit vector n normal to γ, ϕ being constant along it, was written as $n = \nabla\phi/|\nabla\phi|$. It is assumed that $\phi < 0$ inside the drop and $\phi > 0$ outside, so, according to our definition, n points outside the drop. Note that the dynamics of γ is fully described by V_{in} only. In order to follow the evolution of the front it is necessary to extend the normal velocity V_{in} outside the interface. In cases in which the fluid velocity V is continuous across the front, the evolution equation for ϕ can be written as the hyperbolic transport equation

$$\phi_t + V \cdot \nabla\phi - V_{\text{nri}}|\nabla\phi| = 0 \tag{2}$$

where $V_{\text{nri}} = V_{\text{n}} - V_{\text{in}}$ is the fluid normal velocity relative to the interface and $V_{\text{n}} = V \cdot n$. The expression of V_{nri} for the present problem will be given in the next section. Since V_{nri} is defined on the interface only it must be suitably extended off the interface. On the contrary, the first term is naturally extended.

3. MODEL ASSUMPTIONS

The cavity containing the drop and the external liquid matrix is rectangular. The width of the cavity is indicated by L, the height of the cavity by h. A filling ratio F is defined as $F = R^2/hL$. An analogous simulation in cylindrical geometry is under way and will be the object of a forthcoming paper. In the following ∇ indicates the nabla operator, T the temperature, p the average normal stress, ρ the density, c the concentration, λ the thermal conductivity, μ the dynamic viscosity, ν the kinematic viscosity, D the diffusion coefficient, c_{s} the specific heat coefficient, α the thermal diffusivity, σ the interface tension. The transport properties, the specific heat, the density are constant in each phase. The surface phase is modelled as a pure interface. The interface tension is assumed to depend on temperature and equilibrium concentrations as $\sigma = \sigma(T, c^+(T), c^-(T))$. Since the equilibrium concentrations are functions of the temperature, one can expand the interface tension by the chaining rule in terms of the temperature only. Expanding σ in Taylor series and neglecting higher order terms one has

$$\sigma = \sigma_0 + [\sigma_{T0} + \sigma_{c^+0} c^+_{T0} + \sigma_{c^-0} c^-_{T0}](T - T_0) = \sigma_0 + \hat{\sigma}_{T0}(T - T_0) \tag{3}$$

The critical point being singular, a regular truncated Taylor series expansion holds only for $T_0 \neq T_{\text{cr}}$, where $(\mathrm{d}c^{\pm}/\mathrm{d}T)_{\text{cr}} \to \mp\infty$. It must be noted, however, that:

(i) $\sigma_{\text{cr}} = 0$, since, at the critical point, the different phases merge in a single phase,
(ii) a singular behaviour occurs for temperature differences $T - T_{\text{cr}}$ of the order of 10^{-3}°C, when fluctuations are not negligible and critical point phenomena become predominant.

The latter situation can eventually occur at the latest stages of the drop rise, if the critical temperature is reached near the drop surface. The above expression for the interface tension holds outside a small neighbourhood of the critical temperature as

$$\sigma = \sigma_0 + \hat{\sigma}_{T0}(T_{\text{cr}} - T_0) + \hat{\sigma}_{T0}(T - T_{\text{cr}}) = \hat{\sigma}_0 + \hat{\sigma}_{T0}(T - T_{\text{cr}}) \tag{4}$$

Enforcing the interface tension vanishing at the critical point, one has $\sigma = \hat{\sigma}_{T0}(T - T_{\text{cr}})$, $\hat{\sigma}_0 = 0$. According to experimental data [26] $\hat{\sigma}_{T0}$ is negative.

Since cyclohexane and methanol have nearly the same densities and the present problem is related to microgravity conditions, the corresponding density difference is neglected in the

continuity and momentum balance equations and boundary conditions. Buoyancy effects due to density variations in presence of gravity are out of the scope of the present paper, but it will be considered in a forthcoming work.

In jump form the continuity equation at the interface reads

$$[\rho(V_n - V_{\text{in}})] = 0 \tag{5}$$

where $[f] = f^+ - f^-$ is the jump operator and the superscript '+' indicates the domain towards which n points. Mass conservation implies the continuity of the mass flow rate through the interface $\dot{m} = \rho_a(V_{an} - V_{\text{in}})$ $(a = 1, 2)$. Due to the hypothesis $\rho_1 = \rho_2$ the normal component of the velocity is continuous, but differs from the interface normal speed. The tangential speed V_{s} and the temperature T are assumed to be continuous at interface, so the fluid speed is also continuous and Equation (2) holds. The partial mass balance equation in jump form reads

$$[\dot{m}c - n \cdot \rho D \nabla c] = 0 \tag{6}$$

and the mass flow rate is given by

$$\dot{m} = [n \cdot \rho D \nabla c]/[c] \tag{7}$$

where, according to the equilibrium curve, the local concentration jump is function of the temperature. Being $V_{\text{nri}} = \dot{m}/\rho_a$ the level set equation reads

$$\phi_t + V \cdot \nabla\phi - |\nabla\phi|\dot{m}/\rho_a = 0 \tag{8}$$

4. BOUNDARY AND INITIAL CONDITIONS

For $t \geqslant 0$ the velocity vanishes at the cavity walls; the top and bottom walls are held at constant different temperatures T_{t} and T_{b} respectively, with $T_{\text{t}} > T_{\text{b}}$; the lateral walls are adiabatic (i.e. $\partial T/\partial n = 0$); no diffusion of species takes place through the cavity walls (i.e. $\partial c/\partial n = 0$ along the whole boundary). At the initial time the velocity is zero everywhere, the temperature is a linear function of the vertical co-ordinate, the drop is circular with radius R and its centre is located on the symmetry axis at an ordinate y_0. At the initial time the internal and external phases are composed of the single pure components, i.e. $c = 1$ inside the drop and $c = 0$ outside; along the inner and outer drop faces the concentrations are those prescribed by the equilibrium curve at the local temperature. The initial concentration discontinuity between the inner [outer] drop surface and the internal [external] phase is smoothed in few cells by a weighted complementary error function. The initial and boundary conditions are sketched in Figure 2.

5. THE MOTION EQUATIONS

Following Smereka [27] and Sussman *et al.* [19], the motion equations have been reformulated by defining the dependent variables in the whole domain in terms of the Heavyside step function $H(\phi)$, letting $f = (f_{\text{ext}} - f_{\text{int}})H + f_{\text{int}}$ and expressing the interface source terms as

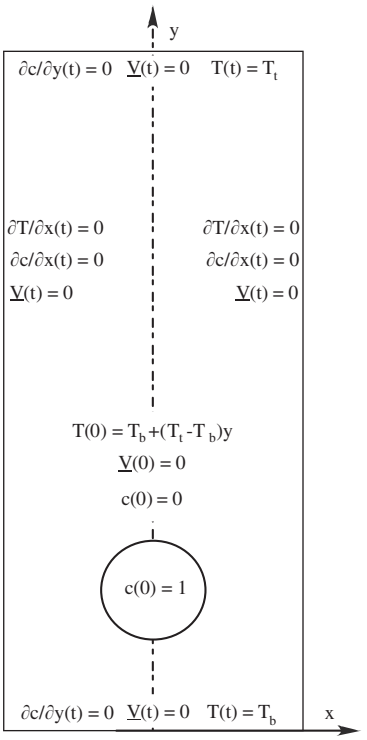

Figure 2. Problem's boundary and initial conditions.

volume source terms thanks to the equality

$$\int_{\partial\gamma} f \,\mathrm{d}\gamma = \int_{\Omega} f|\nabla\phi|\delta(\phi)\,\mathrm{d}\Omega = \int_{\Omega} f n\cdot\nabla H\,\mathrm{d}\Omega \tag{9}$$

where $\nabla H(\phi)=\nabla\phi\delta(\phi)$, $\delta(\phi)$ is the Dirac delta function, Ω is a volume neighbourhood of the zero level set γ, i.e. a strip centred on γ. In the present case the non-dimensional motion equations can be written as

$$\nabla\cdot V = 0 \tag{10}$$

$$\begin{aligned} V_t + \nabla p = {} & \nabla\cdot[\mu(\nabla V + (\nabla V)^{\mathrm{T}})/Re - VV] \\ & + [(T - T_{\mathrm{cr}} - We_{\mathrm{T}}/We)kn - \nabla_{\mathrm{s}}T](n\cdot\nabla H)/We_{\mathrm{T}} \end{aligned} \tag{11}$$

$$(c_{\mathrm{s}}T)_t + \nabla\cdot[c_{\mathrm{s}}TV - \lambda\nabla T/Ma] = 0 \tag{12}$$

$$c_t + \nabla\cdot[Vc - D\nabla c/Re\,Sc] = 0 \tag{13}$$

$$\phi_t + \nabla\cdot(V\phi) - |\nabla\phi|[Dn\cdot\nabla c]/Re\,Sc[c] = 0 \tag{14}$$

where the superscript 'T' indicates transposition, $\nabla_s = \nabla - n\partial/\partial n$ is the surface nabla operator, the non-dimensional density is omitted being uniformly equal to one, the continuity equation multiplied by ϕ has been added to the level equation. The non-dimensional characteristic Schmidt Sc, Reynolds Re, Marangoni Ma, Weber We, thermo-solutal Weber We_T numbers are given by

$$Sc = v_r/D_r \quad Re = RV_r/v_r \quad Ma = RV_r/\alpha_r \quad We = V_r^2\rho_r R/\hat{\sigma}_0 \quad We_T = V_r^2\rho_r R/|\hat{\sigma}_{T0}|T_r \tag{15}$$

where the reference quantities are

$$p_r = \rho_r V_r^2, \quad V_r = |\hat{\sigma}_{T0}|T_r/\mu_r, \quad L_r = R, \quad T_r = (T_t - T_b)R/h, \quad t_r = R/V_r \tag{16}$$

and $c_{sr}, D_r, \lambda_r, \mu_r, \rho_r$ are those of the external fluid. One has $We_T = Re$ and $Ma = PrRe = Pe$, i.e. the Marangoni number is equal to the Peclet number Pe. Terms weighted by Mach and Eckert numbers are neglected. The sign, Heavyside and Dirac delta functions were mollified, respectively as

$$\phi < -\varepsilon\,\mathrm{sgn}_\varepsilon(\phi) = -1, \quad \phi > \varepsilon\,\mathrm{sgn}_\varepsilon(\phi) = 1, \quad |\phi| \leqslant \varepsilon, \quad \mathrm{sgn}_\varepsilon(\phi) = \phi/\varepsilon + \sin(\pi\phi/\varepsilon)/\pi \tag{17}$$

$$H_\varepsilon(\phi) = [1 + \mathrm{sgn}_\varepsilon(\phi)]/2, \quad \delta_\varepsilon(\phi) = \mathrm{d}H_\varepsilon/\mathrm{d}\phi \tag{18}$$

with $\varepsilon = m\Delta x, m = 3$. The drop volume and centre of mass ordinate are given by the following integrals with $m = 1/2$:

$$v = \int\int (1 - H_\varepsilon)\,\mathrm{d}x\,\mathrm{d}y \quad y_{cm} = \left(\int\int y(1 - H_\varepsilon)\,\mathrm{d}x\,\mathrm{d}y\right)/v \tag{19}$$

The trace k of the curvature tensor, is calculated with second order centred formulae, in terms of the level-set function derivatives as

$$k = (\phi_{xx}\phi_y^2 - 2\phi_{xy}\phi_x\phi_y + \phi_{yy}\phi_x^2)/(\phi_x^2 + \phi_y^2)^{3/2} \tag{20}$$

6. THE NUMERICAL SOLUTION METHOD

The system of motion equations in conservative form is solved by a finite volume approach on a staggered grid. The Cartesian grid size is the same in both the co-ordinate directions; pressure, level set function, temperature and concentration are cell centred and the velocity components are staggered. Convective fluxes are evaluated by upwind biased three points formulae with weights given in Shu [28], diffusive fluxes by second order centred formulae. The ordinary projection method of Chorin [15] and Temam [16] is used to determine the velocity field. The pressure Poisson equation is solved by a SOR (successive over relaxations) algorithm. The space semi-discretized motion equations are advanced in time by a first order Euler explicit time stepping.

7. THE REDISTANCING ALGORITHM

Functions d such that $|\nabla d| = 1$ everywhere are called distance functions. Accuracy requires that the level set function ϕ had this property. Even if one initialises ϕ as a distance function,

ϕ can smear out or steep. To ensure that ϕ remains a distance function at least near the interface during its evolution, Sussman *et al.* [19] proposed to reinitialize it at each step by solving the hyperbolic equation to steady state

$$d_\tau = \mathrm{sgn}(\phi)(1 - |\nabla d|), \quad d(x,0) = \phi(x,t) \tag{21}$$

where τ plays the role of a parameter. By rewriting the above equations as

$$d_\tau + \mathrm{sign}(\phi)\,\frac{\nabla d}{|\nabla d|}\cdot\nabla d = \mathrm{sign}(\phi) \tag{22}$$

or

$$d_\tau + \mathrm{sign}(\phi)\left(1 - \frac{1}{|\nabla d|}\right) n_d \cdot \nabla d = 0 \tag{23}$$

one can see that, for the characteristics depart from the interface, the solution tends to the steady state near the interface in few steps since $\varepsilon/\Delta\tau$ time steps are necessary to have $|\nabla d| = 1$ in a neighbourhood of the interface of thickness ε.

The redistancing problem is of Hamilton–Jacoby type

$$d_\tau + H(x, y, \tau, d, d_x, d_y) = 0, \quad d(x, y, 0) = \phi(x, y, t) \tag{24}$$

A semi-discretized approach is used to solve Equations (24). For the space discretization the general Godunov numerical flux function proposed by Osher and Shu [30] is used (the independent variables are omitted for brevity, but their handling is straightforward)

$$\hat{H}^G(u+, u-, v+, v-) = \operatorname*{ext}_{u\in I(u^-,u^+)} \operatorname*{ext}_{v\in I(v^-,v^+)} H(u,v) \quad I(a,b) = [\min(a,b), \max(a,b)] \tag{25}$$

$$\mathrm{ext} = \min_{a\leqslant u\leqslant b} \; a \leqslant b = \max_{b\leqslant u\leqslant a} \; a > b$$

that, in the present case, can be easily calculated, as shown by Jiang and Peng [31], by

$$\begin{aligned}
&\hat{H}^G(u+, u-, v+, v-) \\
&\quad = \mathrm{sign}(\phi)\left(\sqrt{[\max((u^+)^-, (u^-)^+)]^2 + [\max((v^+)^-, (v^-)^+)]^2} - 1\right), \quad \phi \geqslant 0 \\
&\quad = \mathrm{sign}(\phi)\left(\sqrt{[\max((u^+)^+, (u^-)^-)]^2 + [\max((v^+)^+, (v^-)^-)]^2} - 1\right) \quad \phi < 0
\end{aligned} \tag{26}$$

where $u^\pm = d_x^\pm, v^\pm = d_y^\pm, (a)^+ = \max(a,0), (a)^- = -\min(a,0)$ and the superscripts $\pm$ of the derivatives d_x, d_y indicate the upwinding direction. Fifth order WENO (Weighted Essentially Non-Oscillatory) schemes of Jiang and Shu [32] is used for the calculation of the derivatives. Third order TVD (total variation diminishing) Runge–Kutta algorithm of Gottlieb and Shu [33] is used for time integration.

In order to ensure the necessary accuracy of the curvature and to enhance volume conservation during redistancing, the sign function is mollified, as proposed in Peng *et al.* [29]

$$\mathrm{sgn}(\phi) = \phi/\sqrt{\phi^2 + (|\nabla d|\Delta s)^2} \tag{27}$$

This formula prevents errors due to node crossing of the zero level and adapts its support according to the local value of the gradient modulus. The volume preservation algorithm of

Sussman *et al.* [34] is, instead, avoided since it deteriorates the curvature accuracy as noted by Keck [35] and confirmed by numerical tests.

8. THE OFF-INTERFACE EXTENSION

Curvature and temperature, occurring in normal and tangential momentum production terms

$$((T - T_{\mathrm{cr}})/We_{\mathrm{T}} - 1/We)k|\nabla\phi|\delta(\phi)n \quad - (\nabla_{\mathrm{s}}T/We_{\mathrm{T}})|\nabla\phi|\delta(\phi) \tag{28}$$

and the production term of the level set equation

$$|\nabla\phi|\dot{m}/\rho_a \tag{29}$$

have been extended off the interface, following Peng *et al.* [29], then their support is made compact by weighting the extended distributions by a square wave-like filter [29]. Numerical experiments revealed that this procedure greatly enhances the simulation accuracy. If the function $f(\phi)$ is not constant in normal direction near the zero level set, the maximum of the mollified term $f(\phi)\delta_\varepsilon(\phi)$ is not located at 0 on the zero level set and differs from $f(0)\delta_\varepsilon(0)$, this can lead to appearance of spurious vortical structures within the interface strip. Analogously extending off temperature makes vanishing the normal temperature derivative and allows a more accurate evaluation of the tangential stresses contribution. The extension off the interface of the generic quantity f is performed by solving the following Hamilton–Jacoby equation

$$f_\tau + \mathrm{sign}(\phi)n \cdot \nabla f = 0, \quad f(x,0) = f(x,t) \tag{30}$$

At the steady state the function f is constant in the direction of n (in which ϕ varies)

$$n \cdot \nabla f = 0, \quad \nabla\phi \cdot \nabla f = 0 \tag{31}$$

and is equal to the value it has on the zero level set. If f is weighted by a (symmetrically) mollified Dirac function the extrema of the product are all located on the zero level set. If, instead, f is locally monotone around the zero level set the extrema do not fall on it. Extending f off the interface amounts to zeroing its normal derivative so that the gradient ∇f calculated after the extension retains the tangential contribution only. The solution of Equation (30) is performed using formulas similar to those of the previous section with minor modifications.

9. CONCENTRATION FIELD CALCULATION

The normal velocity relative to the interface depends on the difference between the normal derivatives of the concentration and on its jump. This term cannot be easily calculated by means of distributions while retaining the necessary accuracy. In order to evaluate the interface speed an algorithm having a subcell resolution was conceived, following the idea of Harten [36]. The concentration cells intersected by the interface are splitted into two subcells with different averages. From a side the scheme allows to treat finite jumps, from the other the average reconstruction on cells where a jump occurs is not constrained to be only first order accurate.

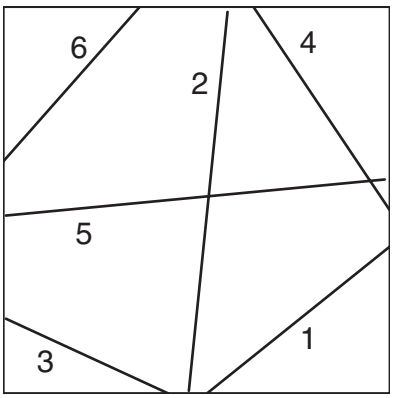

Figure 3. Cell generic partitions.

To locate the interface, the vertex values of the cell centred level set function are calculated by a four point average. The intersection points of the zero level set with the cell edges are determined by linear interpolation along the edges. The interface is represented by the segment joining the two points on the cell boundary. The different generic positions of the interface segment within the cell and the two corresponding subcells are shown in Figure 3. The temperature at intersection points is calculated by a linear interpolation of the vertex values along edges, then the concentration in the same points on each side of the interface is determined by the equilibrium curve.

The cell average increment in each time step is obtained calculating the fluxes across the cell boundary; subcell average increment per time step is obtained evaluating the fluxes across the interface and the portion of the cell boundary bounding the subcell. The normal derivatives to the interface are calculated by a non-constant stencil, average based reconstruction along the normal direction, the stencil fully lying in the external or internal region as appropriate. Stencils extending from the interface in normal direction are truncated if they cross the interface at the opposite side. Two versions of the algorithm have been considered. One performing a truly reconstruction in normal direction, the other performing the reconstruction in the co-ordinate and diagonal directions nearest to the oriented normal and combining them to obtain the relevant quantities along the normal. The velocity on the interface is calculated by imposing the vanishing of mass flux across the subcell boundary. In a similar way, the convective and diffusive normal fluxes along cell edges crossed by the interface are calculated by evaluating the fluxes through each edge portion by a non-constant stencil, upwind biased, average based reconstruction, discussed below, whose stencil lies in the appropriate external or internal region.

The fluxes across the cell edges not crossed by the interface are evaluated by an upwind biased, average based, reconstruction on a three cells stencil. The extrema of the reconstruction subintervals are the cell boundaries if the stencil is not crossed by the interface. In the case in which the interface crosses one of the cells of the three-point stencil but does not cross the cell edge where the flux is reconstructed, the stencil may be limited by one or two interface points. If the interface intersects the line connecting the stencil cell centres in the reconstruction direction, the stencil subinterval is limited by the intersection point of this line

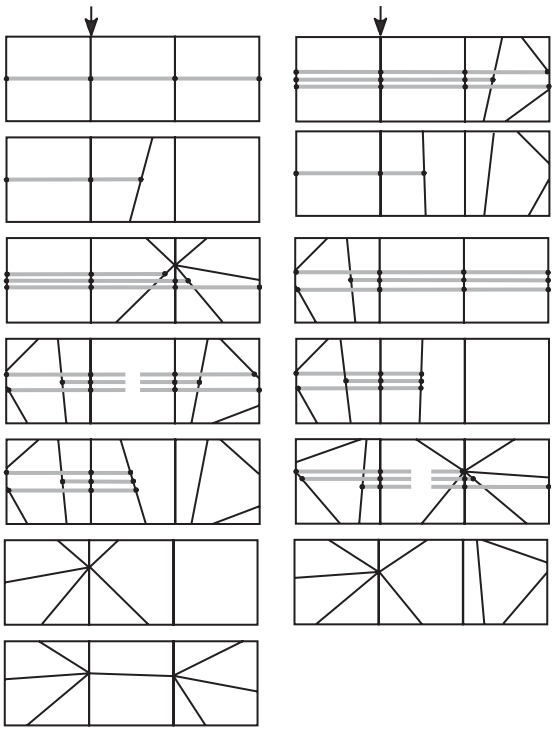

Figure 4. Interface location and reconstruction stencil in contiguous cell.

and the interface segment otherwise the reconstruction subinterval extrema are on the cell boundary. Since only averages from one side of the interface may enter in the reconstruction, the number of considered averages can be smaller than three. Diffusive fluxes are calculated in terms of the derivative of the reconstruction polynomial evaluated on the cell edge. The possible interface segments disposition in three contiguous cells and the corresponding stencil supports (in grey) for the flux reconstruction through a cell wall non intersected by the interface (indicated by an arrow), are shown in Figure 4. Here the velocity comes from right, opposed direction upwinding is treated similarly. In the case in which the interface crosses the cell edge on which the flux is being reconstructed, the fluxes across these edge portions are calculated in a way similar to the one discussed before, but now the points bounding the reconstruction subintervals are located along the normal to the edge portion passing through its centre. Various reconstructions of mixed type on variable stencils, involving averages and known interface point values, have been tested but they show to be more prone to non-monotone behaviour (oscillations) than average based ones.

For the subcell dimensions vary in a time step due to the interface motion, the time increment of the subcell averages is computed by a Lagrangian balance. The first order time discretized subcells and cell balances read

$$v_s^{n+1}\overline{\rho c}_s^{n+1} - v_s^n\overline{\rho c}_s^n = -\left[\int_{\partial v_{te}} n_e \cdot \left(\rho c V - \frac{\rho D}{Re\,Sc}\nabla c\right) \mathrm{d}\partial v\right]^n \Delta t - \overline{f_s^n}|g|S_l\Delta t \tag{32}$$

$$v_c^{n+1}\overline{\rho c}_c^{n+1} - v_c^n\overline{\rho c}_c^n = -\left[\int_{\partial v_{ce}} n_e \cdot \left(\rho c V - \frac{\rho D}{Re\,Sc}\nabla c\right) \mathrm{d}\partial v\right]^n \Delta t - \overline{f_c^n}|g|S_l\Delta t \tag{33}$$

$$v^{n+1}\overline{\rho c}^{n+1} - v^n\overline{\rho c}^n = -\left[\int_{\partial v_e} n_e \cdot \left(\rho c V - \frac{\rho D}{Re\,Sc}\nabla c\right) \mathrm{d}\partial v\right]^n \Delta t \tag{34}$$

where the overbar indicates the average, the subscripts 's' and 'c' indicate a subcell and its complement respectively, the subscript 'e' a part of the cell boundary and n_e the cell exiting normal unit vector. The factor $|g| = |1 \pm \mathrm{d}nS_l/4A_t|$ $[|g| = 1]$ for triangular [quadrilateral] subcells, where S_l and A_t are the interface segment length and the area of the subcell at time n, $\mathrm{d}n = |\overline{V_{n,\mathrm{int}}}|^n \Delta t$ and the sign $+$ $[-]$ is used for $V_{\mathrm{int}} \cdot n_s > 0$ $[< 0]$. The fluxes are given by $\bar{f}_s = -\bar{f}_c = \pm f^{\pm}$ for $n_e = \pm n_s$, where $f^{\pm} = (\dot{m}c - \rho D c_{n_e}/Re\,Sc)^{\pm}$. The product $|g|S_l$ approximates the volume spanned by the interface in a time step in the hypothesis that it moves normally to itself. A better approximation can be achieved by inserting in the above balances the volume variation $v_{s,c}^{n+1} - v_{s,c}^n$ directly.

Once the product $v_s^{n+1}\overline{\rho c}_s^{n+1}$ has been determined, since v_s^{n+1} can be calculated from ϕ^{n+1}, one can recover the mass fraction average for unit volume as

$$\overline{\rho c}_s^{n+1} = v_s^{n+1}\overline{\rho c}_s^{n+1}/v_s^{n+1} \tag{35}$$

The average $\overline{\rho c}_c^{n+1}$ in the complementary subcell, of volume v_c^{n+1}, can be obtained combining the balance in the subcell with the one of the entire cell

$$v_c^{n+1}\overline{\rho c}_c^{n+1} = v\overline{\rho c}^{n+1} - v_s^{n+1}\overline{\rho c}_s^{n+1} \quad v_c^{n+1} = v - v_s^{n+1} \quad \overline{\rho c}_c^{n+1} = v_c^{n+1}\overline{\rho c}_c^{n+1}/v_c^{n+1} \tag{36}$$

Inspired by Almgren *et al.* [37], strong stability constraints coming from very small subcell dimensions, that are in some sense generic, are overcame by letting the subcell average equal to the mean value of the concentrations in the extrema of the interface segment bounding the subcell taken on the proper side.

Ad hoc structures are defined to manage quantities and variables of cells intersected by the interface. Particular care must be used at each time step in redefining structures and data when the interface enters or leaves a cell and when a subcell changes is kind (see Figure 3). Due to the cumbersome management of such structures when a multi-level time integration is used, time advancing was performed with an explicit first order Euler scheme. The implementation of higher order TVD Runge–Kutta algorithms for the non-dissolving drop case is in progress.

The normal derivatives of the concentration at the inner and outer drop face are also used in the calculation of the mass flow through the interface as defined in Section 3. The mass flow, before being inserted in the production term of the level equation, was extended off the interface as discussed in the previous section.

It is perhaps useful to write down explicitly the local mass fraction flux through the interface

$$f^{\pm} = \frac{1}{Re\,Sc}\frac{1}{(c_e - c_i)}\left[\left(\rho D\frac{\partial c}{\partial n}\right)_e c_i - \left(\rho D\frac{\partial c}{\partial n}\right)_i c_e\right] \tag{37}$$

and comparing it with the mass flux

$$\dot{m} = \frac{1}{Re\,Sc}\frac{1}{(c_e - c_i)}\left[\left(\rho D\frac{\partial c}{\partial n}\right)_e - \left(\rho D\frac{\partial c}{\partial n}\right)_i\right] \tag{38}$$

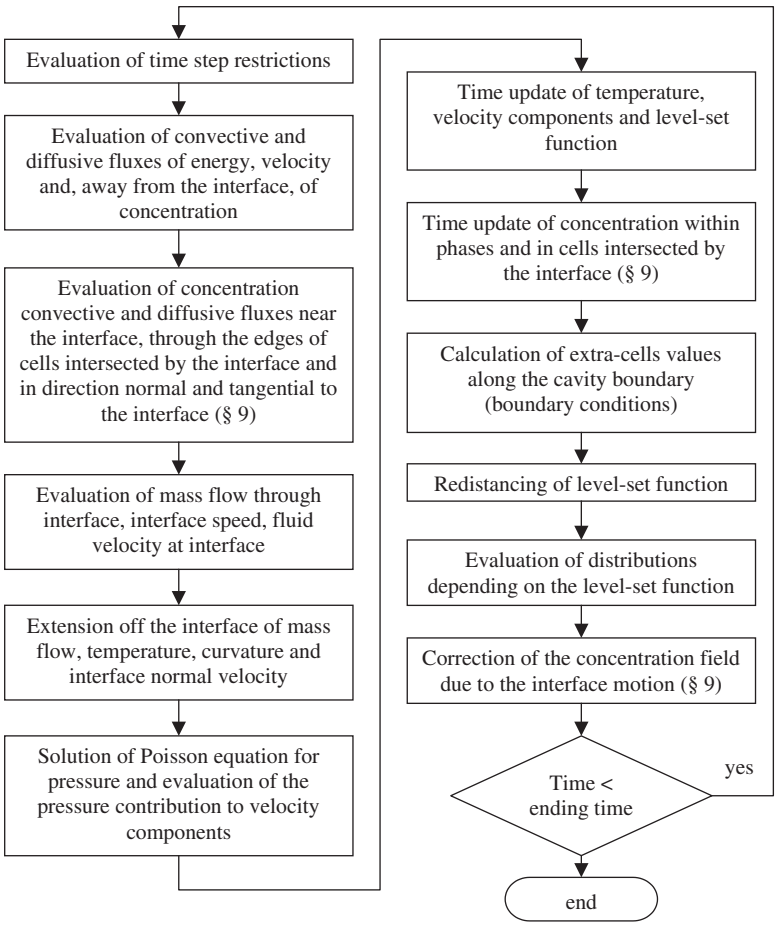

Figure 5. Flow diagram summarizing the steps taken in the numerical algorithm.

The above formulas show that the terms occurring in $\dot{m}$ and $f^{\pm}$ are the same but differently weighted, thus the two fluxes may or may not have different signs, depending on the actual value of the weights. For the reader's convenience, a flow chart summarizing the steps taken in the numerical algorithm is shown in Figure 5.

10. RESULTS

The grid is composed by 120×240 squared cells. The cavity is 3 cm wide and 6 cm high. At the initial time the drop centre is located on the symmetry axis. Very long execution times prevent us from using more refined grids. The considered drop radii are $R = 0.25$, 0.5 and 0.75 cm, and the corresponding filling factor F is 3.472e-3, 1.388e-2, 3.125e-2, respectively. The drop centre distance from the lower wall is 0.75 cm for the first two radii and 1 cm for the last one. The lower wall temperature is 15°C, the upper wall one is 55 or 65°C.

Table I. Main properties of Cyclohexane and Methanol. Dimensional quantities are in cgs units. The interfacial tension gradient has been measured at MARS laboratory [26].

	Cyclohexane C_6H_{12}	Methanol CH_3OH	f_{int}/f_{ext}
ρ	0.779	0.779	1
μ	0.980e-2	0.790e-2	0.806
ν	1.258e-2	0.998e-2	0.806
λ	1.248e4	2.020e4	1.619
c_s	1.859e7	2.533e7	1.362
D	1.000e-5	1.000e-5	1
Pr	1.460e1	9.904	0.678
Sc	1.258e3	1.014e3	0.806
σ_T	-1.000e-2		—

Table II. Steady migration velocities and non-dimensional parameters for different runs. Calculated speed values are compared to corresponding analytical values, determined by Young *et al.* [3], in the case of Stokes flow ($Re \ll 1$).

R (cm)	ΔT (°C)	Re	Ma	Re_{int}	Ma_{int}	Present (cm/s)	[3] (cm/s)
0.25	40	34	493	42	414	0.043	0.255
0.25	50	42	617	52	519	0.056	0.319
0.5	40	135	1974	168	1661	0.065	0.510
0.5	50	169	2467	210	2076	0.076	0.638
0.75	40	304	4441	377	3737	0.038	0.765
0.75	50	380	5551	472	4672	0.052	0.957

Accordingly the imposed temperature difference ΔT is 40 or 50°C, for a total of six different runs. Initially the temperature profile is linearly stratified, the drop is of pure methanol and the surrounding matrix of pure cyclohexane, i.e. the methanol mass fraction is one in the drop and zero outside, both phases are quiescent.

The fluid properties used for simulations are reported in Table I, where the subscript 'int' indicates internal quantities. Non-dimensional parameters and characteristic numbers depending only on fluid properties are also reported there. The internal and external Reynolds and Marangoni numbers are listed, for each run, in Table II.

During the initial stage of motion the fluid is dragged along the drop surface by the interface tension, the dragged fluid is warmer than the one inside the drop that remains trapped. The external fluid, instead, creates a warm wake that extends behind the drop and entrains the cold bottom region. This qualitative pattern is similar in all cases and is shown in Figure 6 for $R = 0.75$ and $\Delta T = 50$°C, after $t = 4.7$ s from the staring time. The inner flow reaches the drop rear pole, starts to rise along the symmetry axis, reaches the front pole and then flows back, creating a ring vortex inside the drop, as shown f.i. in Figure 7 for the case $R = 0.5$, $\Delta T = 40$°C at $t = 17.6$ s. After a sudden acceleration, the drops start to move with a velocity that first decreases with increasing the time and then increases towards a steady value as shown by the slope of the drop centre position curves versus time shown in Figure 8. In the initial phase of the ascent, larger drops are shrunk along the symmetry axis and then return to be nearly circular, as shown in Figure 9 for the case $R = 0.75$ and $\Delta T = 50$°C where the drop shape

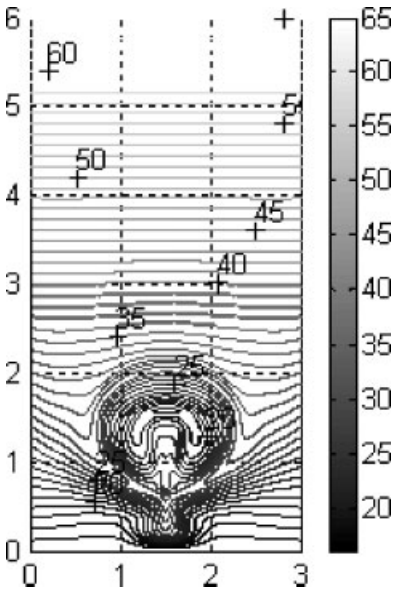

Figure 6. Isotherms at $t = 4.7$ s, for $R = 0.75$ cm, $\Delta T = 50^{\circ}$C. The warmer fluid is dragged along the interface by interface tension and entrains the cold bottom region of the cavity.

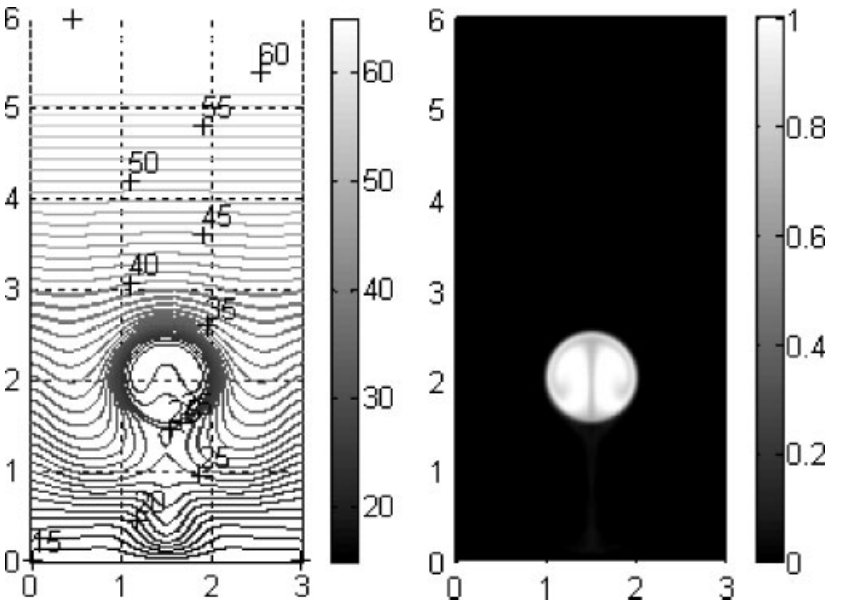

Figure 7. Isotherms (left) and concentration (right) field at $t = 17.6$ s for $R = 0.5$ cm, $\Delta T = 50^{\circ}$C.

is depicted for $t = 3.528$ s and $t = 7.056$ s. After the start-up phase the drops decelerate and acquire a steady migration speed, as shown by Figure 8. During their ascent the drops slowly warm up due to the large Prandtl numbers listed in Table I. Temperature and concentration

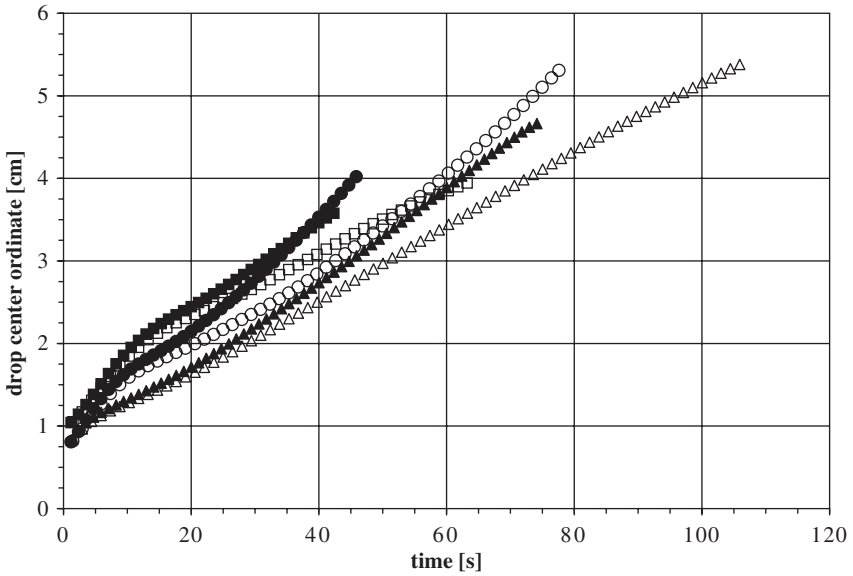

Figure 8. Drop centre position versus time for $R = 0.25$ (△), 0.5 (◯), 0.75 (□) cm and $\Delta T = 40$ (white symbols), 50 (black symbols) °C.

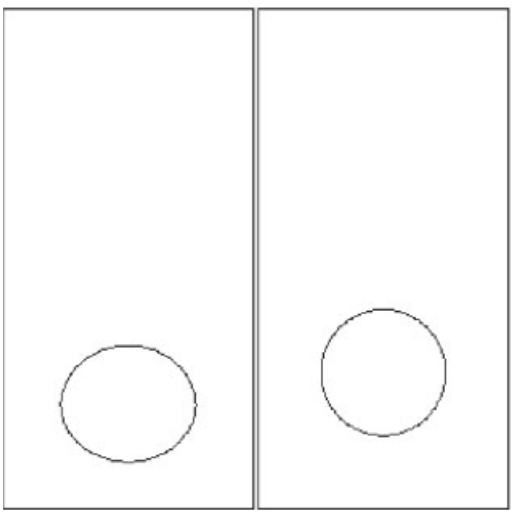

Figure 9. Larger drops are shrinked at start-up. The two images refer to $t = 3.53$ s (left) and $t = 7.06$ s (right) for $R = 0.75$ cm, $\Delta T = 50°C$.

fields at $t = 41.2$ s for $\Delta T = 40°C$ and $R = 0.25$, 0.5, 0.75 cm are shown in Figure 10. The steady migration velocity values are reported in Table II. As expected the velocity increases with increasing the imposed temperature difference and with increasing the drop radius. The present values are compared with the corresponding ones obtained by means of analytical

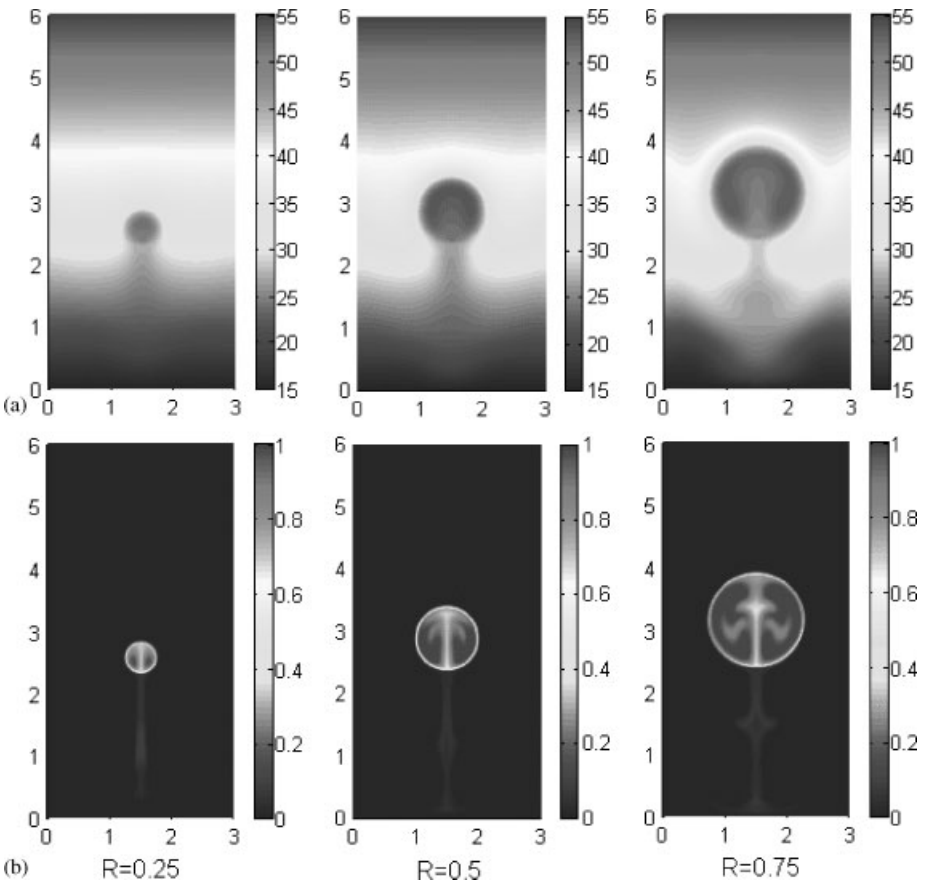

Figure 10. Temperature (a, up) and concentration (b, down) fields at $t = 41.2$ s for $\Delta T = 40°C$ and $R = 0.25$ (left), 0.5 (centre), 0.75 (right) cm.

solution [3] holding for low Reynolds number flows. Similarly to the case of thermo-capillary bubble migration [6], the present values of the steady migration velocities are one order of magnitude lower than those obtained for $Re \ll 1$. The migration speeds, non-dimensionalized with respect to the characteristic velocity $V_{ygb} = (2R|\sigma_T|\Delta T/\mathrm{h})/[(2\mu + 3\mu_{\mathrm{int}})(2 + \lambda_{\mathrm{int}}/\lambda)]$ [3], are plotted versus the Marangoni number Ma in Figure 11. It must be noted, however, that largest drops, after the transient initial phase, reach a migration velocity that is lower than that of medium size drops subjected to the same temperature difference. This occurrence can be explained by observing that the thermal field in the wall region remains almost unperturbed in the case of small or medium drops while for largest drops the stratified temperature profile near the walls is highly distorted by capillary convection, so that drops do not migrate as in an unbounded medium of infinite extent subjected to a temperature gradient uniform at infinity as shown in Figure 10(a).

At high Reynolds numbers the isotherms tend to fold over the drop. In the case $R = 0.75$ cm, at about $t = 47$ s for $\Delta T = 40°C$ and at $t = 38$ s for $\Delta T = 50°C$, the temperature ceases to

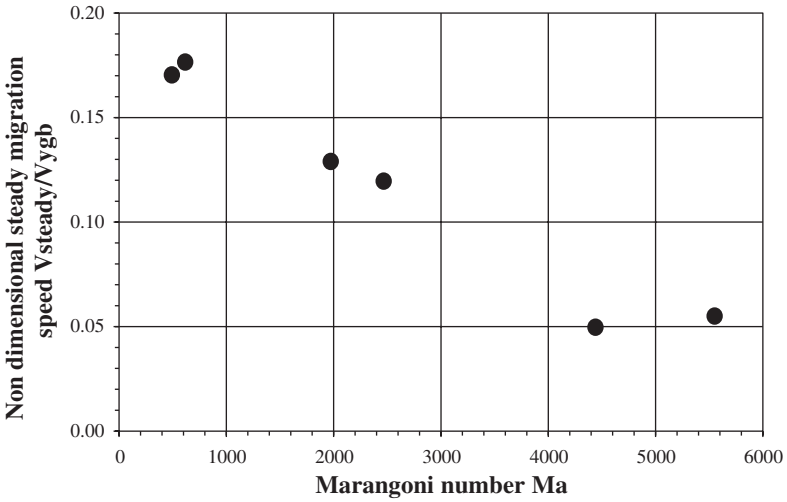

Figure 11. Non-dimensional migration speed versus the external Marangoni number *Ma*.

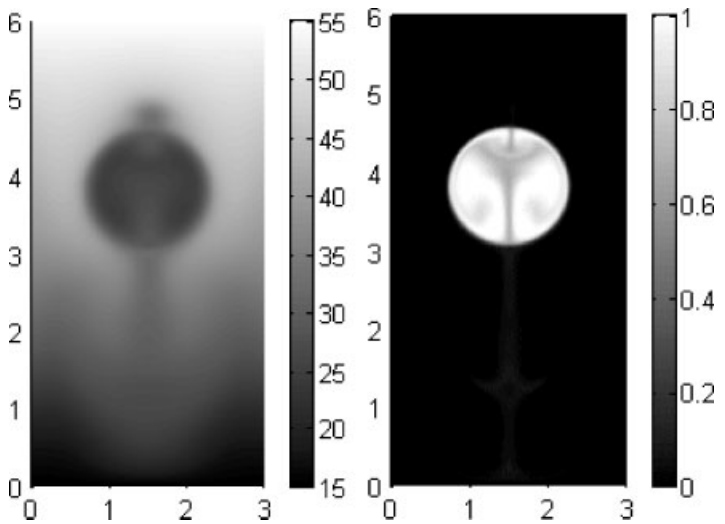

Figure 12. Temperature (left) and concentration (right) fields at $t = 58.8$ s for $R = 0.75$ cm, $\Delta T = 40°$C.

decrease monotonically along the drop surface and the interface tension maximum ceases to be located on the symmetry axis. This leads to the inversion of the direction of the interface tension near the interface fore pole. The inverted flow region grows rapidly and gives rise to a second, counter-rotating, vortex within drop. The outer fluid in the front of the drop is pushed up and the inner fluid is pushed down as clearly indicated by temperature and concentration fields of Figure 12 at $t = 58.8$ s for $\Delta T = 40°$C. The global trust due to

capillary forces then reduces and the drop slows down. The development of this pattern is probably due to the coarseness of the grid that should be refined to avoid the growth of such disturbances. It must be taken into account, however, that a similar behaviour can also occur in laboratory experiment, the thermal gradient being not perfectly stratified or the drop migrating in a perturbed environment (f.i. the wake of a preceding drop), especially at high transport numbers as the ones considered here. In some experiments on thermo-capillary migration of bubbles and drops [7, 38, 39] migration was not observed or strong speed reduction of drops migrating in the wake of a preceding drop have been reported [7]. These behaviours could be explained in terms of a local inversion of the surface temperature gradient.

Information on flow evolution is also provided by the concentration field, which is also driven by dissolution. According to initial conditions and equilibrium curve, the concentration decreases going from the inner phase to the inner surface of the drop and still decreases going from the outer face towards the external phase. The internal vortical flow that establishes after the start-up, is characterized near the drop surface and along the axis by concentration values lower than those of the ring vortex core. This is obviously due to the fact that the low concentration masses of fluids are those that have been convected along the interface where the concentration is fixed by the equilibrium curve, as clearly evidenced in Figure 10(b). The concentration field follows the qualitative evolution of the thermal field even if the diffusion of specie is sensibly lower than that of energy, the Schmidt numbers being larger than the Prandtl numbers. Similarly, the outer capillary flow drags more concentrated fluid masses in the wake. The mass fraction distributions of Figure 10(b) show how, after a complete tour of the fluid inside the drop, the inner low and outer high concentration regions become larger due to the depletion or enrichment of the fluid along the interface, as one can see by observing by the concentration distribution near the axis or in the wake. It must be noted that low concentrated masses rising along the drop are convected downward by the vortex ring axis before reaching the front pole and the interface.

As shown by the same figure, the mass fraction of the external phase changes slightly and in the wake only, due to the very low diffusion coefficient and to the low values of the concentration along the left branch of the equilibrium curve of Figure 1. As seen, the mass fraction variations are instead appreciable within the drop, where the values change form the initial unit ones, persisting on the vortex ring centre, to values lower than 0.7 at the drop inner surface. Differently from the case of the mass flow through the interface discussed below, no conclusions on the sign of the concentration flux can be drawn *a priori*, since the two terms of Equation (38) are about of the same order of magnitude at the initial time. The positiveness of the concentration flux through the interface during migration is revealed by the already noted increase of the concentration outside the drop and in the wake.

In the present problem the volume flow through the drop interface is proportional to the mass flow, the phases being isodense and the flow incompressible. The local mass flow through interface $\dot{m}$, according to Equation (7), is proportional to the difference of the concentration normal derivatives and inversely proportional to the concentration jump, which depends on the local temperature and goes to zero at the critical point. Thus, according to Figure 1, the denominator of $\dot{m}$ is always negative, the concentration of methanol being larger in inner phase. An increase of temperature can cause an increase of the intensity of $\dot{m}$ but not a sign change. At initial time normal derivatives are both negative. The initial conditions and the equilibrium curve make the inner normal derivative, in modulus, fairly larger than the external one, of about an order of magnitude. This leads to the conclusion that at least

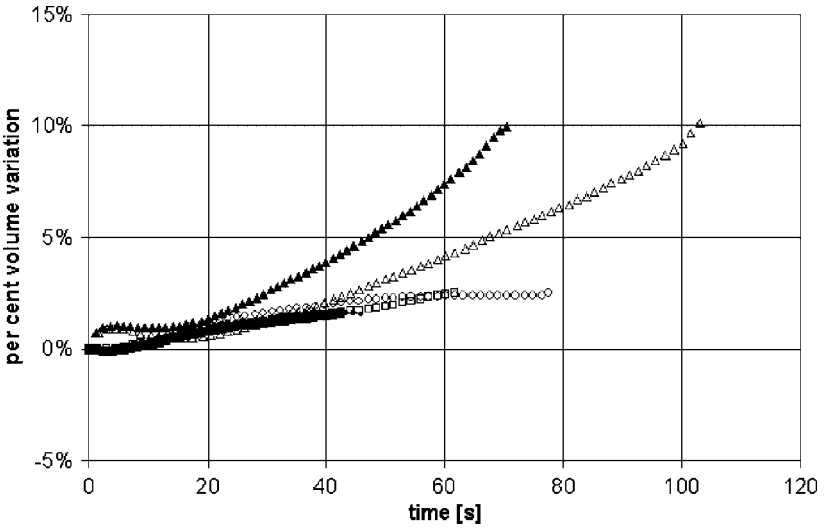

Figure 13. Relative volume variation versus for $R = 0.25$ (△), 0.5 (◯), 0.75 (□) cm and $\Delta T = 40$ (white symbols), 50 (black symbols) °C.

for short times the drop volume should increase. In absence of convection, volume variation should occur in times of the order of the diffusive characteristic time R^2/D and volume should increase for quite long times. This initial portrait is influenced by two factors. The first is the decrease of the inner concentration with increasing the temperature, which, according to the equilibrium diagram, tends to increase the modulus of the inner (negative) normal derivative. The second and opposite factor is the decrease of the average concentration within the drop due to convection, by Marangoni effect, of low concentrated masses of fluid coming from the interface and of their subsequent diffusion. This diffusive effect tends to reduce indirectly the modulus of the inner derivative. Both these perturbations act in characteristic convective times. These perturbations act also outside the drop. The (negative) external normal derivative tends to increase in modulus, due to the increase in temperature, and is slightly affected by Marangoni convection, since the external flow comes from a region at constant concentration.

It is worthy to note that an exchange of inner and outer components should lead to an initial volume decrease, and probably monotone in time, instead of an increase, $\dot{m}$ being positive at the initial time. The drop relative volume variation $(v - v(0))/v(0)$ is plotted versus time in Figure 13. The effect of dissolution on volume variation is quite limited except in the case of small drops. Medium and large drops slightly grow while smaller drops grow faster. This different behaviour can be explained in terms of temperature and concentration pattern evolution.

At start-up the drop cold core is wrapped by the warmer fluid dragged by interface tension along its surface. Since the energy exchange by heat between the drop and the surrounding phase is very small, the drop tends to stay cold. Accordingly, the external isotherms encountered by the drop during the ascent do not penetrate within the drop and fold over it. The drop pushes the isotherms up and constrains them in a narrow thermal boundary layer, surrounding the drop and having a steep normal temperature gradient, as shown in Figure 10(a). Therefore

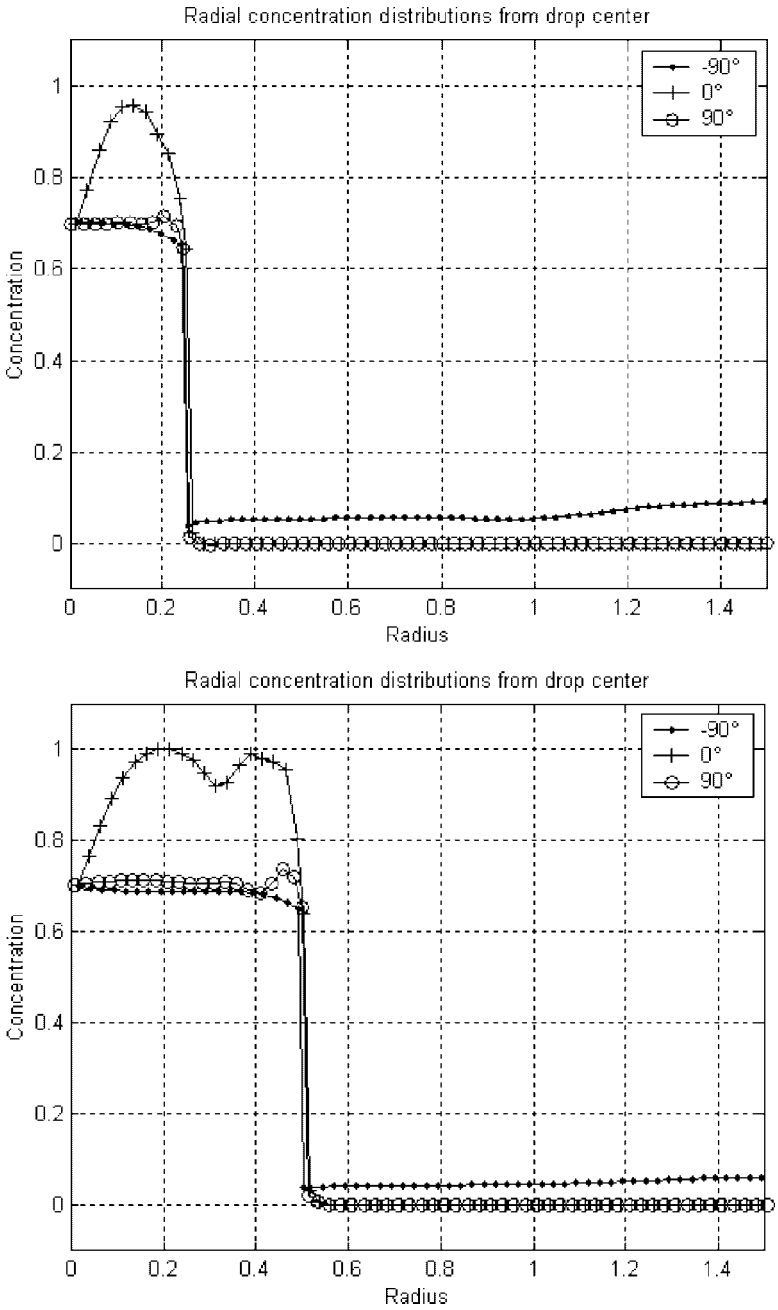

Figure 14. Concentration profiles in planes passing through the drop centre of mass and inclined at 90, 0, $-90°$, at $t = 42.6$ s for $R = 0.25$ cm, $\Delta T = 40°$C (up) and $R = 0.5$ cm, $\Delta T = 40°$C (down).

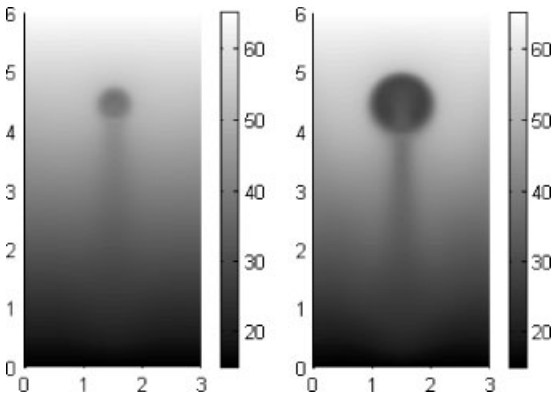

Figure 15. Temperature fields at $t = 69.4$ s, for $\Delta T = 50^{\circ}$C, $R = 0.25$ cm (left) and at $t = 50.3$ s for $R = 0.5$ cm, $\Delta T = 50^{\circ}$C (right).

the temperature on the drop surface does not change appreciably during the rise and remains lower than the one corresponding to the unperturbed stratified profile at the actual height. Correspondingly the concentration jump neither goes to zero neither decreases appreciably and the mass flow rate through the interface remains bounded also in the upper part of the cavity, where the unperturbed temperature is higher than the critical one.

In Figure 14 the concentration profiles in planes passing through the cell centre nearest to the drop centre of mass and inclined at 90°, 0°, -90° with respect to the horizontal are plotted for $t = 42.6$ s, $R = 0.25$, 0.5 and $\Delta T = 40^{\circ}$C. Here the displacement of the interface position in different sections is mainly due to the fact that intersection planes are not exactly barycentric. The remarkable differences in the concentration profiles within the drop are due to the fact that the ± 90 profiles lie along the axis, where the low concentration fluid coming from the drop inner surface rises, pushed by the inner Marangoni flow, while the 0° profile cuts the high concentration region of the ring vortex core. The difference of the outer concentration profiles is due to the fact that the 90 and 0° profiles extend in unperturbed regions while the -90° profile extends in the wake.

By comparing the slopes at the interface one deduces that the mass flow through the interface is negative and that the drop tend to increase in volume. These two facts agree with and explain the slow volume growth of medium and large drops. In the case of small drops, instead, even if energy diffusion is quite limited, it is nevertheless sufficient to reduce drop temperature, due to the reduced drop dimensions. This is shown in Figure 15. Here the temperature fields around a small and a medium drop at about the same height, for $\Delta T = 40^{\circ}$, are compared. One must also consider that the migration of small drops is slower and the drop has a larger time to adequate itself to the external conditions. The increase of the drop surface temperature, through the concentration jump at the interface, leads to a volume variation, shown in Figure 13, faster and larger than that of bigger drops.

11. CONCLUSIONS

In the present paper the thermo-solutal-capillary multiphase flow of a binary mixture exhibiting a miscibility gap is numerically investigated. A fixed grid level-set based algorithm is used

in order to follow the drop motion allowing it to deform freely. A high order redistancing algorithm is used to enhance the accuracy of the level-set approach. In order to obtain an accurate evaluation of the volume production terms, coming from the level-set formulation of the boundary conditions between different phases, an algorithm is designed for the correct location of distributions on the zero level-set, mollification, extension and filtering of the quantities related to such terms. It is noteworthy that in the present paper both tangential stresses and mass flow through the interface are considered. In order to simulate the dissolution process, an algorithm having subcell resolution is set up for the mass fraction equation. It allows accurate jumps description, has relaxed stability requirements and is able to calculate an interface velocity depending on difference of normal derivatives of a discontinuous function. Numerical simulations show that the interface jump is quite well resolved. The code models both the transient start-up phase and the following quasi-steady migration, taking into account the effects of boundary walls, for different drop dimensions and applied thermal gradients. The thermo-fluid dynamic field evolution is discussed on the basis of the obtained numerical results.

ACKNOWLEDGEMENTS

The author is indebted to Profs. Osher, Shu, Zhao and Dr.s Jiang, Peng, Keck for their invaluable help. The paper has been developed under ASI contract.

REFERENCES

1. Predel B, Ratke L, Fredriksson H. In *Fluid Science and Materials Science in Space*. Walter HU (ed). Springer: Berlin, 1987.
2. Ratke L. In *Immiscible Liquid Metals and Organics*. DGM Informationsgesellshaft, 1993.
3. Young NO, Goldstein JS, Block MJ. The motion of bubbles in a vertical temperature gradient. *Journal of Fluid Mechanics*. 1959; **6**:350–356.
4. Bratukhin YK. Thermocapillary drift of a drop of viscous liquid. *Iz. Ak. Nauk SSSR, Mekh. Zhid. i Gaza* 1975; **5**:157–161.
5. Szymczyk J, Siekmann J. Numerical calculation of the thermocapillary motion of a bubble under microgravity. *Chemical Engineering Communication* 1988; **69**:129–147.
6. Balasubramanian R, Lavery J. Numerical simulation of thermocapillary bubble migration under microgravity for large Reynold and Marangoni numbers. *Numerical Heat Transfer* Part A, 1989; **16**:175–187.
7. Balasubramanian R, Lacy C, Wozniak G, Subramanian S. Thermocapillary migration of bubbles and drops at moderate values of the Marangoni number in reduced gravity. *Physics of Fluids* 1996; **8**:872–880.
8. Haj-Hariri H, Shi Q, Borhna A. Thermocapillary motion of deformable drops at finite Reynolds and Marangoni numbers. *Physics of Fluids* 1997; **9**:845–855.
9. Harlow FH, Welch JE. Numerical calculations of time dependent viscous compressible flow of fluid with free surfaces. *Physics of Fluids* 1965; **8**:2182–2189.
10. Hirt CW, Nichols BD. Volume of Fluid (VOF) Method for the Dynamics of Free Boundaries. *Journal of Computational Physics* 1981; **39**:201–225.
11. Unverdi OS, Tryggvason G. A front tracking method for viscous incompressible flows. *Journal of Computational Physics* 1992; **100**:25–37.
12. Baker GR, Moore DW. The rise and distortion of a two-dimensional gas bubble in an inviscid liquid. *Physics of Fluids A* 1989; **1**:1451–1459.
13. Scardovelli R, Zaleski S. Direct numerical simulation of free surface and interfacial flow. *Annual Reviews of Fluid Mechanics* 1999; **31**:567–603.
14. Brackbill JU, Kothe DB, Zemach C. A continuous method for modeling surface tension. *Journal of Computational Physics* 1992; **100**:335–354.
15. Chorin AJ. Numerical solutions of the Navier Stokes equations. *Mathematics of Computing* 1968; **23**:341–354.
16. Temam R. Sur l' approximasion de la solution de l' equations de Navier–Stokes par la méthode des pas fractionnaire. *Archives of Rational Mechanics and Analysis* (I) 1969; **32**:135–53; (II) 1969; **33**:377–385.

17. Bell JB, Marcus DL. A second order Projection method for variable density flows. *Journal of Computational Physics* 1992; **101**:334–348.
18. Osher S, Sethian J. Fronts propagating with curvature-dependent speed: algorithms based on Hamilton–Jacobi formulation. *Journal of Computational Physics* 1988; **79**:12–49.
19. Sussman M, Smereka P, Osher S. A level set approach for computing solutions to incompressible two-phase flow. *Journal of Computational Physics* 1994; **114**:146–159.
20. Beux F, Knowlton B, Banerjee S. A tridimensional level set method for direct simulation of two-phase flows in variable gravity environments. *Proceedings of the 1998 Fourth Microgravity Fluids Physics and Transport Phenomena Conference*, 12–14 August 1998, Cleveland, Ohio, USA.
21. Tryggvason G, Juric D, Che J, Nobari MRH, Nas S. *Computations of Multiphase Flows by a Finite Difference/Front Tracking Method. III Variable Surface Tension and Phase Change. 29th Computational Fluid Dynamics Lecture Series* 1998-03. Von Karman Institute for Fluid Dynamics.
22. Brackbill JU, Juric D, Torres D, Kallman E. Dynamic modeling of microgravity flow. *Proceedings of the 1998 Fourth Microgravity Fluids Physics and Transport Phenomena Conference*, 12–14 August 1998, Cleveland, Ohio, USA.
23. Esmaeeli A, Arpaci V. Numerical modeling of three-dimensional fluid flow with phase change. *Proceedings of the 1998 Fourth Microgravity Fluids Physics and Transport Phenomena Conference*, 12–14 August 1998, Cleveland, Ohio, USA.
24. Nobari MR, Jan YJ, Tryggvason G. Head-on Collision of Drops—A Numerical Investigation. *Physics of Fluids* 1996; **8**:29–42.
25. Esmaeeli A, Tryggvason G. Direct numerical simulations of bubbly flows. Part I low Reynolds number arrays. *Journal of Fluid Mechanics* 1998; **377**:313–345, Part II moderate Reynolds number arrays. *Journal of Fluid Mechanics* 1999; **385**:325–358.
26. Bassano E, Castagnolo D, Albano F. Thermocapillary two-phase flow of a binary mixture drop exhibiting a miscibility gap. IAF-01-J.4.09, 52-th IAF congress, 1–5 Oct. 2001, Tolouse, France.
27. Smereka P. Level set methods for two-fluid flows. INRIA short course lecture notes.
28. Shu CW. High order ENO and WENO schemes for computational fluid dynamics. In *Advanced Numerical Approximation of Nonlinear Hyperbolic Equations*. Quarteroni A (ed.), *Lecture Notes in Mathematics*, vol. 1697. Springer: Berlin, 1998.
29. Peng D, Merriman B, Osher S, Zhao H, Kang M. A PDE-based fast local level set method. *Journal of Computational Physics* 1999; **155**:410–438.
30. Osher S, Shu CW. High-order essentially nonoscillatory schemes for Hamilton-Jacobi equations. *SIAM Journal on Numerical Analysis* 1991; **28**:907–922.
31. Jiang G-S, Peng D. Weighted ENO schemes for Hamilton-Jacobi equations. *SIAM Journal on Scientific Computing* 2000; **21**:2126–2143.
32. Jiang G-S, Shu CW. Efficient implementation of weighted ENO schemes. *Journal of Computational Physics* 1996; **126**:202–228.
33. Gottlieb S, Shu CW. Total variation diminishing Runge–Kutta schemes. *Mathematics of Computing* 1998; **67**:73–85.
34. Sussman M, Fatemi E, Smereka P, Osher S. An improved level set method for incompressible two-phase flows. *Computers and Fluids* 1998; **27**:663–680.
35. Keck R. Reinitialization for level-set methods. Diploma Thesis, University of Kaiserlautern, 1998.
36. Harten A. ENO schemes with subcell resolution. *Journal of Computational Physics* 1989; **83**:148–184.
37. Almgren AS, Bell JB, Colella P, Marthaler T. A Cartesian grid projection method for the incompressible Euler equations in complex geometries. *SIAM Journal on Scientific Computing* 1997; **18**:1289–1309.
38. Papazian JM, Wilcox WR. Interaction of bubbles with solidification interfaces. *AIAA Journal* 1978; **16**:447–451.
39. Neuhaus D, Feuerbacher B. Bubble motions induced by a temperature gradient. *Proceedings of the 6th European Symposium on Material Sciences under Microgravity Conditions*, Bordeaux, France, December 2–5, 1986, ESA SP 256, 241–244.

